



## Article

# Assembling Ultrafine SnO<sub>2</sub> Nanoparticles on MIL-101(Cr) Octahedrons for Efficient Fuel Photocatalytic Denitrification

Ruowen Liang<sup>1,2</sup>, Shihui Wang<sup>1,3</sup>, Yi Lu<sup>1,3</sup>, Guiyang Yan<sup>1,2,4</sup> , Zhoujun He<sup>1,2</sup>, Yuzhou Xia<sup>1,2,\*</sup>, Zhiyu Liang<sup>1,2,\*</sup>  and Ling Wu<sup>3,\*</sup>

<sup>1</sup> Province University Key Laboratory of Green Energy and Environment Catalysis, Ningde Normal University, Ningde 352100, China; t1629@ndnu.edu.cn (R.L.); wangshihui21@163.com (S.W.); luyi080391@163.com (Y.L.); ygyfjnu@163.com (G.Y.); hhzzjj1990@163.com (Z.H.)

<sup>2</sup> Fujian Provincial Key Laboratory of Featured Materials in Biochemical Industry, Ningde Normal University, Ningde 352100, China

<sup>3</sup> State Key Laboratory of Photocatalysis on Energy and Environment, Fuzhou University, Fuzhou 350002, China

<sup>4</sup> Xiamen Ocean Vocational College, Xiamen 361000, China

\* Correspondence: yzxia@ndnu.edu.cn (Y.X.); lzyfjnu@yeah.net (Z.L.); wuling@fzu.edu.cn (L.W.); Tel.: +86-593-2965018 (Y.X.); +86-593-2954127 (Z.L.); +86-591-83779105 (L.W.)

**Abstract:** Effectively reducing the concentration of nitrogen-containing compounds (NCCs) remains a significant but challenging task in environmental restoration. In this work, a novel step-scheme (S-scheme) SnO<sub>2</sub>@MCr heterojunction was successfully fabricated via a facile hydrothermal method. At this heterojunction, MIL-101(Cr) octahedrons are decorated with highly dispersed SnO<sub>2</sub> quantum dots (QDs, approximate size 3 nm). The QDs are evenly wrapped around the MIL-101(Cr), forming an intriguing zero-dimensional/three-dimensional (0D/3D) S-scheme heterostructure. Under simulated sunlight irradiation (280 nm < λ < 980 nm), SnO<sub>2</sub>@MCr demonstrated superior photoactivity toward the denitrification of pyridine, a typical NCC. The adsorption capacity and adsorption site of SnO<sub>2</sub>@MCr were also investigated. Tests using 20%SnO<sub>2</sub>@MCr exhibited much higher activity than that of pure SnO<sub>2</sub> and MIL-101(Cr); the reduction ratio of Cr(VI) is rapidly increased to 95% after sunlight irradiation for 4 h. The improvement in the photocatalytic activity is attributed to (i) the high dispersion of SnO<sub>2</sub> QDs, (ii) the binding of the rich adsorption sites with pyridine molecules, and (iii) the formation of the S-scheme heterojunction between SnO<sub>2</sub> and MIL-101(Cr). Finally, the photocatalytic mechanism of pyridine was elucidated, and the possible intermediate products and degradation pathways were discussed.

**Keywords:** MIL-101(Cr); SnO<sub>2</sub>; photocatalysis; pyridine; denitrification



**Citation:** Liang, R.; Wang, S.; Lu, Y.; Yan, G.; He, Z.; Xia, Y.; Liang, Z.; Wu, L. Assembling Ultrafine SnO<sub>2</sub> Nanoparticles on MIL-101(Cr) Octahedrons for Efficient Fuel Photocatalytic Denitrification. *Molecules* **2021**, *26*, 7566. <https://doi.org/10.3390/molecules26247566>

Academic Editor: Wing-Kei Ho

Received: 19 November 2021

Accepted: 10 December 2021

Published: 14 December 2021

**Publisher's Note:** MDPI stays neutral with regard to jurisdictional claims in published maps and institutional affiliations.



**Copyright:** © 2021 by the authors. Licensee MDPI, Basel, Switzerland. This article is an open access article distributed under the terms and conditions of the Creative Commons Attribution (CC BY) license (<https://creativecommons.org/licenses/by/4.0/>).

## 1. Introduction

Liquid fuels are widely used in electricity and transportation systems. Crude gasoline fuel naturally contains high concentrations of nitrogen-containing compounds (NCCs) such as pyridine, indoles, nitrides, and their derivatives. The combustion products (e.g., NO<sub>x</sub> and unburned hydrocarbon particles) are released into the environment, causing photochemical smog and exerting serious hazardous effects on ecosystems and human health [1,2]. As environmental regulations become more stringent, the removal of NCCs from fuel has become increasingly more important. To meet the quality demands of liquid fuels with low nitrogen content, the nitrogen species can be removed by catalytic hydrodenitrification (HDN). In fact, HDN is regarded as the classic technology of nitrogen-species removal from fuels [3] but requires high temperatures, high pressures, and very active catalysts. Current research has focused on photocatalytic one-pot removal of NCCs, mainly because the involved reactions are “green”, mild, and directly utilize sunlight. Thus far, only a few semiconductors such as Bi<sub>20</sub>TiO<sub>32</sub>, TiO<sub>2</sub>/Fe<sub>2</sub>O<sub>3</sub>, and Bi<sub>2</sub>MoO<sub>6</sub>/CdS

have been explored as fuel denitrification photocatalysts [4–7]. Exploring more effective photocatalysts for gasoline fuel denitrification remains among the most attractive topics in fuel purification research.

Metal-organic frameworks (MOFs), a class of crystalline porous materials with tailored pores/structures and high surface areas, have attracted great interest in various fields [8]. Owing to their high specific surface area, adjustable pore size, and easily modified surfaces, MOFs are strong candidates for photocatalysis [9–12]. The application of MOFs as photocatalysts was reported as early as 2004 by Garcia et al. [13]. Many MOFs, for example, MIL-125(Ti)-NH<sub>2</sub>, MIL-68(In)-NH<sub>2</sub>, MIL-53(Fe), and MIL-101(Cr), possess the semiconductor characteristics required of photocatalysts [14–17]. However, the deficient active sites and low separation efficiency of the photoinduced carriers reduce the photocatalytic performance of pure MOFs [18,19]. To further improve their photoactivities, many researchers proposed to construct MOFs-based heterostructures, such as Type-II heterojunction, Z-scheme heterojunction, and step-scheme (S-scheme) heterojunction [20–23]. Our group has also designed a novel sandwich-like hierarchical AgBr-Ag@MIL-68(Fe) S-scheme photocatalyst with excellent photocatalytic activity for Cr(VI) reduction and dye degradation [11].

SnO<sub>2</sub>, a chemically stable n-type semiconductor with an approximate bandgap energy of 4.0 eV, has attracted much interest for its superior photocatalytic oxidation performance. This high performance is attributable to the valence band (VB) edge of SnO<sub>2</sub>, which is located at ca. 3.9 eV vs. NHE [24,25]. However, the slow electron transfer dynamics and weak reduction potentials of the conduction band (CB) electrons (with energy levels of ca. -0.1 eV vs. NHE) restrict the applications of SnO<sub>2</sub> in photocatalytic reactions. S-scheme coupling promises to overcome the drawbacks of SnO<sub>2</sub> and MOFs by deliberately sacrificing the holes and electrons with poor redox ability and retaining those with strong redox ability. However, the existing reports on SnO<sub>2</sub>@MOFs have focused only on lithium-ion batteries or electrochemical sensing [26,27]; reports on SnO<sub>2</sub>@MOFs for photocatalytic applications are rather scarce. MOF-based S-scheme photocatalysts for fuel denitrification are unavailable at present.

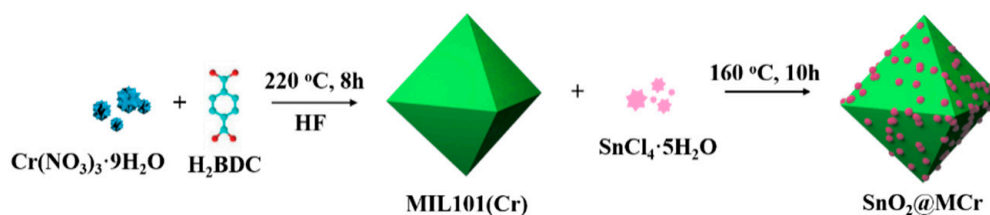
MIL-101(Cr) (Cr<sub>3</sub>F(H<sub>2</sub>O)<sub>2</sub>O[(O<sub>2</sub>C)C<sub>6</sub>H<sub>4</sub>(CO<sub>2</sub>)<sub>3</sub>.nH<sub>2</sub>O, *n* ≈ 25) is a Cr-based MOF synthesized by G. Férey et al. in 2005 [28]. In previous work, it was chosen as the target supporter owing to its high chemical stability, water stability, and photoresponsiveness [29–32]. Inspired by the unique features of MIL-101(Cr), we designed a zero-dimensional/three-dimensional (0D/3D) S-scheme heterojunction involving MIL-101(Cr) octahedrons decorated with SnO<sub>2</sub> quantum dots (QDs) (denoted by SnO<sub>2</sub>@MCr). The first fabrication step prepares the MIL-101(Cr) octahedrons. Next, SnO<sub>2</sub> quantum dots (QDs or nanoparticles) are anchored on the rhombic octahedral MIL-101(Cr) crystals via a facile in situ hydrothermal strategy. The photocatalytic activities of the as-prepared SnO<sub>2</sub>@MCr samples are investigated in the denitrification of pyridine, a typical NCC, under simulated sunlight irradiation (280 nm < λ < 980 nm). The decomposition process of pyridine and the formation of intermediate products are systematically investigated, and the surface microstructure of the photocatalyst is related to its photocatalytic performance. Finally, the possible mechanism of the decomposition process is deduced.

## 2. Results

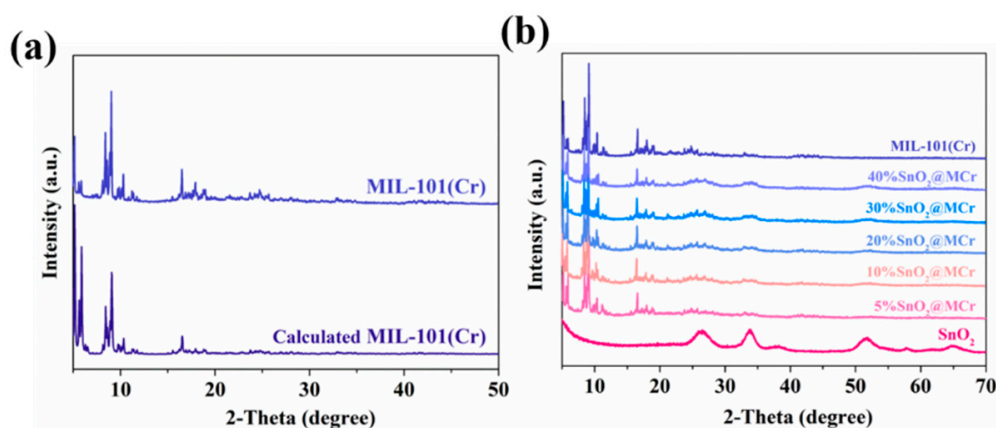
### 2.1. Characterizations

A series of SnO<sub>2</sub>@MCr composites was prepared via a two-step synthetic procedure (see Scheme 1). Figure 1a shows the XRD patterns of the as-prepared samples. All diffraction peaks of the MIL-101(Cr) sample were well matched to the calculated peaks, indicating the successful synthesis of MIL-101(Cr) materials [28,30]. The diffraction peaks at 2θ = 27.14°, 34.87°, and 52.74° in Figure 1b were consistent with the diffractions of the (110), (101), and (211) planes of tetragonal SnO<sub>2</sub>, respectively (JCPDS no. 00-021-1250) [24,25]. Meanwhile, all characteristic diffraction peaks of SnO<sub>2</sub> and MIL-101(Cr) were found in the SnO<sub>2</sub>@MCr composites, indicating the successful introduction of SnO<sub>2</sub> on the MIL-101(Cr)

architecture. The diffraction intensity of MIL-101(Cr) in the nanocomposite gradually weakened from that of pure MIL-101(Cr) as the loading amount of SnO<sub>2</sub> QDs increased, suggesting a covering effect. Moreover, the characteristic peaks of the SnO<sub>2</sub> QDs were rather flatter than those of pure SnO<sub>2</sub>. Using the Debye–Scherrer equation [33], this flattening can be ascribed to the small size and highly uniform distribution of the SnO<sub>2</sub> QDs on the MIL-101(Cr) surfaces. In an inductively coupled plasma–atomic emission spectrometry analysis, the amounts of SnO<sub>2</sub> doped on the MIL-101(Cr) surface were confirmed as 4.33, 9.21, 17.64, 27.74, and 37.65 wt.%, slightly lower than their theoretical values of 5, 10, 20, 30, and 40 wt.%, respectively.



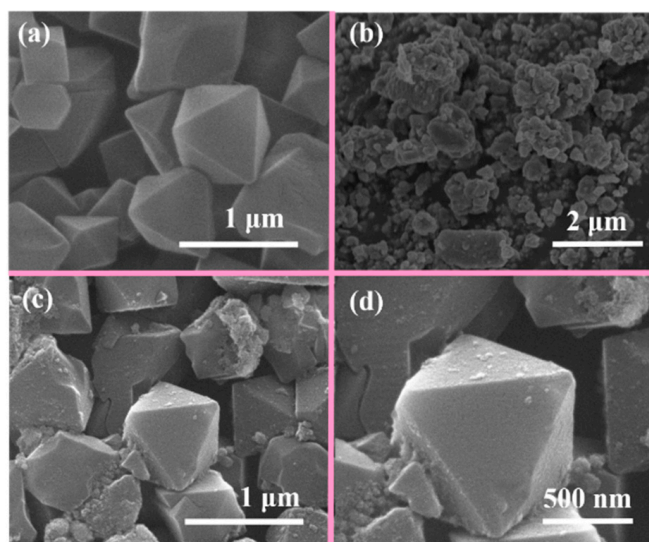
**Scheme 1.** Flow diagram of the fabrication of SnO<sub>2</sub>@MCr samples.



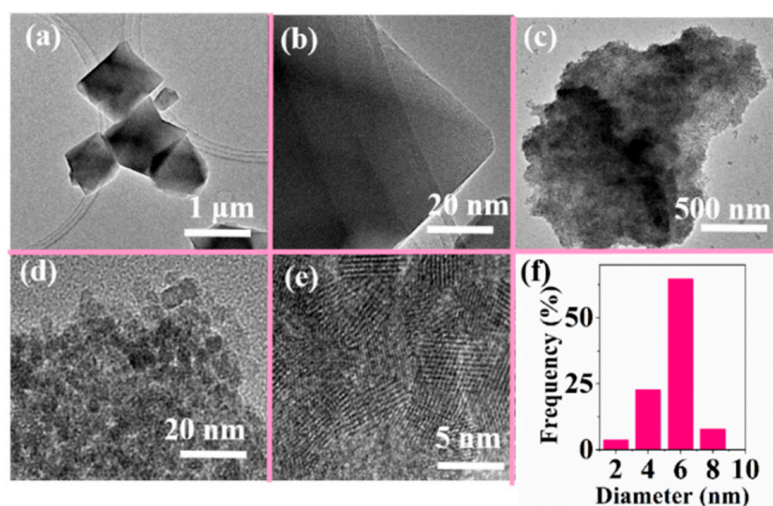
**Figure 1.** XRD patterns of the (a) as-prepared and calculated MIL-101(Cr), (b) XRD patterns of MIL-101(Cr), SnO<sub>2</sub>, and SnO<sub>2</sub>@MCr samples.

Figure S1 (in Supplementary Material) shows the Fourier transform infrared (FTIR) spectra of the samples. In the spectra of MIL-101(Cr), the peaks at 1402, 1622, and 1709 cm<sup>−1</sup> were attributed, respectively, to the aromatic O=C=O, C–C, and C–O stretching vibration modes of the H<sub>2</sub>BDC ligand, respectively [34]. The characteristic peak pair in the 800–500 cm<sup>−1</sup> range typified the absorption peaks of Cr–O. In the spectrum of SnO<sub>2</sub>, the bands between 800 and 500 cm<sup>−1</sup> were ascribed to the stretching vibrations of Sn–O [24]. Since SnO<sub>2</sub> contains no special functional groups on its surface, the FTIR spectrum of 20%SnO<sub>2</sub>@MCr was similar to that of MIL-101(Cr), further implying that the MIL-101 (Cr) structure was maintained after the hydrothermal process.

The morphologies of the samples were investigated by scanning electron microscopy (SEM). Pure MIL-101(Cr) exhibited a diagnostic octahedral structure and smooth surface (Figure 2a), whereas SnO<sub>2</sub> appeared as irregular nanoparticles (Figure 2b). The particles of SnO<sub>2</sub>@MCr were shaped similarly to those of MIL-101(Cr), but the smooth surfaces of the MIL-101(Cr) octahedrons were roughened after introducing the SnO<sub>2</sub> (Figure 2c,d), because they were distinctly covered by uniform SnO<sub>2</sub> clusters. The microstructures of the SnO<sub>2</sub>@MCr composites were further investigated through transmission electron microscopy (TEM) and high-resolution TEM (HRTEM) analyses. The pure MIL-101(Cr) sample exhibited an octahedral microstructure with an approximate particle diameter of 600 nm (Figure 3a,b). Pure SnO<sub>2</sub> presented a quasi-spherical morphology consisting of agglomerated particles with a mean diameter of 5–6 nm (Figure 3c–f).



**Figure 2.** Selected micrographs of SEM of the indicated samples: (a) MIL-101(Cr), (b) SnO<sub>2</sub>, and (c,d) 20%SnO<sub>2</sub>@MCR.



**Figure 3.** TEM images of (a,b) MIL-101(Cr) and (c–e) SnO<sub>2</sub>, and (f) the corresponding size distribution of SnO<sub>2</sub>.

Taking 5%SnO<sub>2</sub>@MCR composite as an example, the SnO<sub>2</sub> particles, when grown on MIL-101(Cr), were highly dispersed, and the SnO<sub>2</sub> QDs were tightly wrapped around the MIL-101(Cr) surface (Figure 4a–c). Note that the octahedral morphology of MIL-101(Cr) was maintained after growing SnO<sub>2</sub> in situ. In the representative HRTEM image of SnO<sub>2</sub> (Figure 4d), the lattice fringes were separated by 0.34 nm. This spacing corresponds to the interplanar distance of the (110) planes of tetragonal SnO<sub>2</sub>. Unlike pure SnO<sub>2</sub>, the SnO<sub>2</sub> QDs in the SnO<sub>2</sub>@MCR composites with approximate diameters of 3–5 nm were highly dispersed on the MIL-101(Cr) surface (Figure 4e). No agglomerates or isolated SnO<sub>2</sub> clusters were detected in the nanocomposites. This uniformity can be attributed to the high specific surface area of MIL-101(Cr), enabling control of the morphology and particle size of SnO<sub>2</sub>. As for the samples of 10%SnO<sub>2</sub>@MCR and 20%SnO<sub>2</sub>@MCR, increasing the amount of SnO<sub>2</sub> increased the coverage of SnO<sub>2</sub> QDs on the MIL-101(Cr) surface and reduced the size of the SnO<sub>2</sub> QDs (Figure 4f–o), which may be attributed to the augmentation of the interface contact area between MIL-101(Cr) and SnO<sub>2</sub>. However, an aggregating phenomenon appeared when the SnO<sub>2</sub> amount was increased to 30 wt.% (Figure 4p–y).



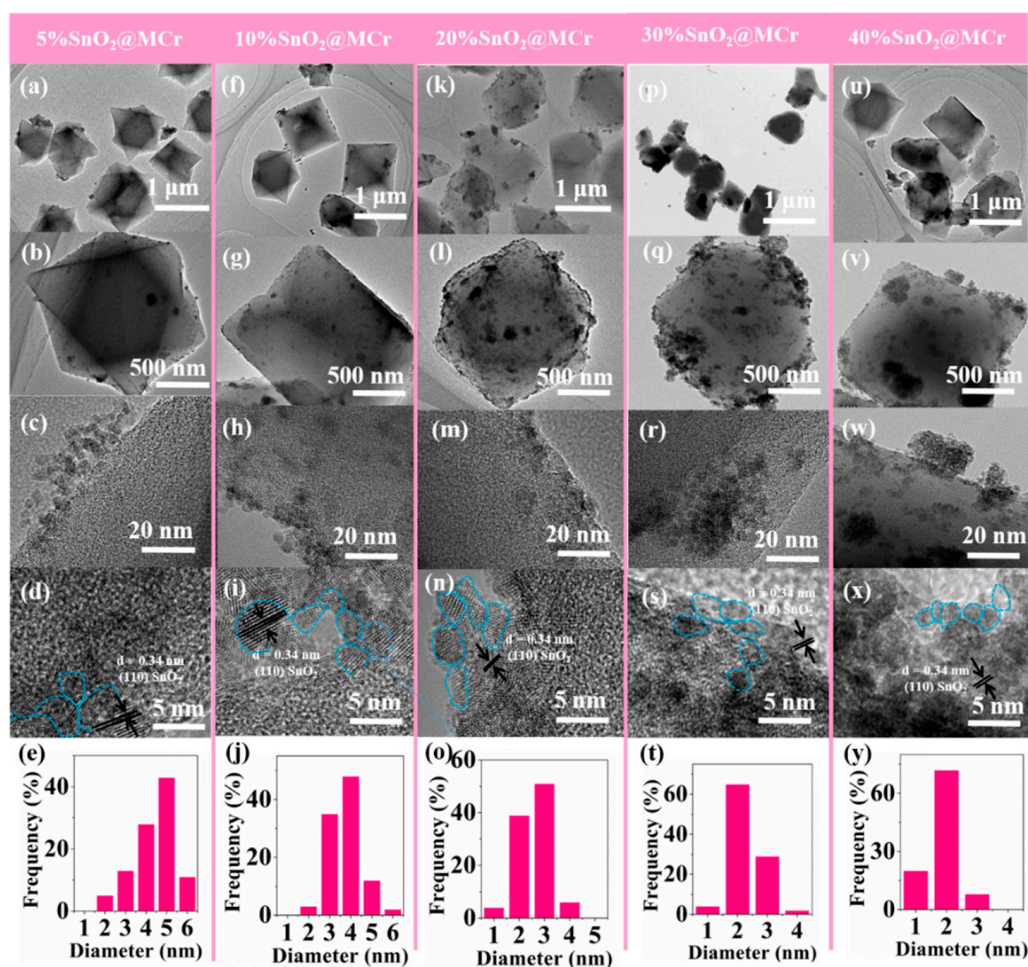


**Figure 4.** Transmission electron microscopy (TEM) images of (a–d) 5%SnO<sub>2</sub>@MCR, (f–i) 10%SnO<sub>2</sub>@MCR, (k–n) 20%SnO<sub>2</sub>@MCR, (p–s) 30%SnO<sub>2</sub>@MCR, and (u–x) 40%SnO<sub>2</sub>@MCR; the corresponding size distributions of SnO<sub>2</sub>s in the samples of (e) 5%SnO<sub>2</sub>@MCR, (j) 10%SnO<sub>2</sub>@MCR, (o) 20%SnO<sub>2</sub>@MCR, (t) 30%SnO<sub>2</sub>@MCR, and (y) 40%SnO<sub>2</sub>@MCR.

The spatial distributions and elemental compositions of the samples were analyzed by energy-dispersive X-ray spectroscopy (EDS). The full EDS spectrum of 20%SnO<sub>2</sub>@MCR is shown in Figure S2a. The spectrum presents the signal peaks of C, Cr, O, and Sn, confirming the existence of the prepared MIL-101(Cr) and SnO<sub>2</sub> in the composite samples. As further evidence, the EDS mapping images (Figure S2b–d) displayed the homogeneous distribution of C, O, Cr, and Sn elements through the composite, illustrating that SnO<sub>2</sub> was successfully loaded on MIL-101(Cr) to form a heterogeneous structure.

The surface compositions and chemical states of the samples were elucidated by X-ray photoelectron spectroscopy (XPS). The survey XPS spectrum (Figure 5a) of SnO<sub>2</sub>@MCR was dominated by C, O, Cr, and Sn, consistent with the EDS results. Meanwhile, the C 1s spectrum of MIL-101(Cr) showed three peaks at 284.46, 285.34, and 288.57 eV, corresponding to C–C/C=C, C–O, and C=O of H<sub>2</sub>BDC, respectively [34,35] (Figure 5b). The two peaks at 587.16 and 577.69 eV in Figure 5c were attributed to the 2p<sub>1/2</sub> and 2p<sub>3/2</sub> signals of Cr, respectively, demonstrating the presence of Cr<sup>3+</sup> in MIL-101(Cr) [35]. Importantly, the dominant peaks of C 1s and Cr 2p in the spectrum of the SnO<sub>2</sub>@MCR sample shifted to higher binding energies from those of pure MIL-101(Cr). The corresponding binding energies are summarized in Table 1. In the high-resolution Sn 3d XPS spectrum of pure SnO<sub>2</sub> (Figure 5d), the binding energies at 487.36 and 495.73 eV were assigned to 3d<sub>5/2</sub> and 3d<sub>3/2</sub> of Sn, respectively, indicating the presence of Sn<sup>4+</sup>. In the Sn 3d spectrum of the SnO<sub>2</sub>@MCR sample, the Sn 3d<sub>5/2</sub> and Sn 3d<sub>3/2</sub> peaks shifted to 487.19 and 496.19 eV,

respectively, from those of SnO<sub>2</sub>. This shift was accompanied by a lower-energy shift of the Cr 2p and C 1s peaks, indicating a decreased electron density on the Cr and C moieties and an increased electron density on the Sn moieties, while a built-in electric field formed at the SnO<sub>2</sub>@MnCr interface [36]. Collectively, these results indicate a strong interaction between SnO<sub>2</sub> and MIL-101(Cr) in SnO<sub>2</sub>@MnCr rather than a simple physical mixture. All XPS results implied that SnO<sub>2</sub> QDs were successfully loaded on the MIL-101(Cr) surface, thus fabricating the S-scheme SnO<sub>2</sub>@MnCr photocatalytic system.

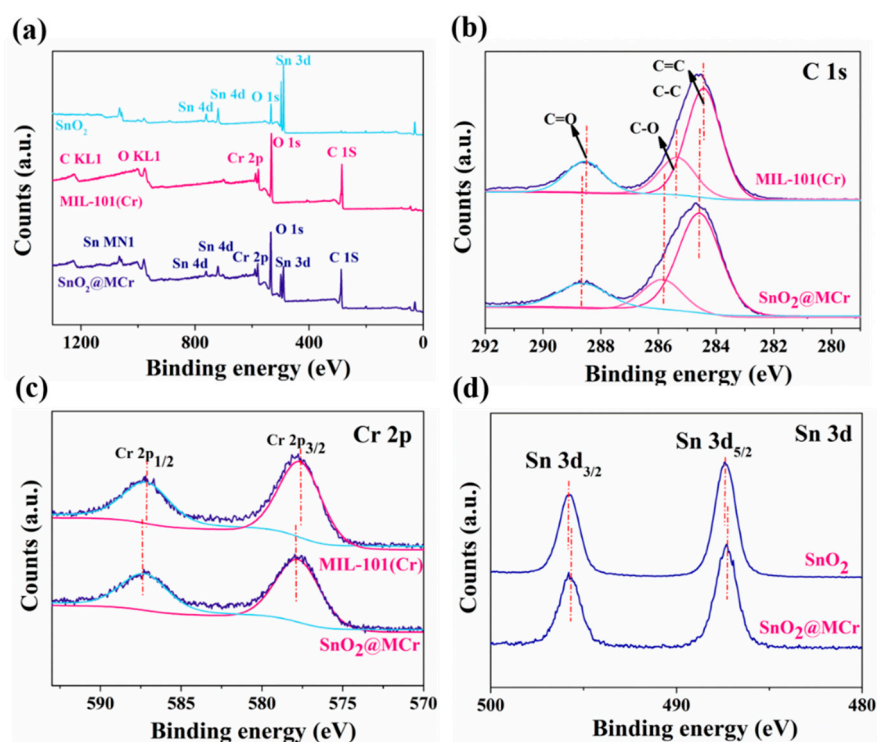


**Figure 5.** X-ray photoelectron spectroscopy (XPS) spectra of the samples: (a) survey spectra, (b) C 1s, (c) Cr 2p, and (d) Sn 3d.

**Table 1.** XPS binding energies of the as-synthesized photocatalysts.

Title 1	MIL-101(Cr)	SnO <sub>2</sub>	20%SnO <sub>2</sub> @MnCr
C Banding energy (eV)	284.46		284.58
	285.34	N/A	285.87
	288.57		288.64
Cr Banding energy (eV)	577.69	N/A	577.75
	587.16		587.26
Sn Banding energy (eV)	N/A	487.36 eV	487.19
		495.73 eV	495.19

The Brunauer–Emmett–Teller (BET) surface areas and pore structures of the prepared samples were determined from adsorption–desorption measurements and are displayed in Figure 6a,b. The nitrogen adsorption–desorption isotherm of the original MIL-101(Cr) was a type I isotherm on the IUPAC classification scheme. Together with the corresponding pore-size distribution, this result indicates a mesoporous structure [34] (Figure 6b). Table 2 lists the surface areas and pore volumes of the samples. The BET surface area and pore volume of MIL-101(Cr) were 3834 m<sup>2</sup>/g and 1.66 cm<sup>3</sup>/g, respectively. When the SnO<sub>2</sub> QDs were introduced, they occupied the pores of MIL-101(Cr), so the BET surface area and pore volume decreased. However, they still exceeded those of the SnO<sub>2</sub> sample (pore volume = 161 m<sup>2</sup>/g; see Figure S3).

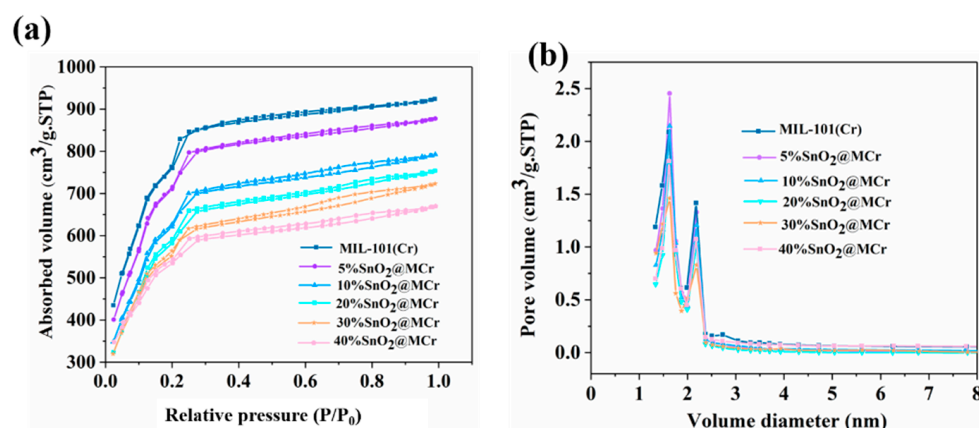


**Figure 6.** (a) Nitrogen sorption isotherms and (b) pore size distributions of MIL-101(Cr) and SnO<sub>2</sub>@MCR.

**Table 2.** BET surface areas and pore volumes of the as-synthesized photocatalysts.

Sample	BET Surface Area (m <sup>2</sup> /g)	Pore Volume (cm <sup>3</sup> /g)
MIL-101(Cr)	3834	1.66
5%SnO <sub>2</sub> @MCR	3434	1.55
10%SnO <sub>2</sub> @MCR	2985	1.40
20%SnO <sub>2</sub> @MCR	2828	1.34
30%SnO <sub>2</sub> @MCR	2565	1.26
40%SnO <sub>2</sub> @MCR	2299	1.08
SnO <sub>2</sub>	161	0.10

Figure 7a shows the optical absorption spectra of all samples. The spectrum of pure SnO<sub>2</sub> displayed an absorption edge around 370 nm. The spectrum of pristine MIL-101(Cr) exhibited intense absorption in both the UV and visible regions, with two characteristic peaks. The absorption band of MIL-101(Cr) in the UV region was assigned to  $\pi$ - $\pi^*$  transitions of the ligands and Cr (III)-oxide clusters, whereas the visible-light absorption came from Cr<sup>3+</sup>-oxide clusters, which characteristically absorbed at 450 and 600 nm (as also reported in the literature [17,34,37]). In the spectra of the SnO<sub>2</sub>@MCR samples, the absorption edge of SnO<sub>2</sub> was undisturbed after the SnO<sub>2</sub> QDs was grown on the on MIL-101(Cr), possibly because the SnO<sub>2</sub> QDs could not alter the crystal lattice of MIL-101(Cr) [38]. The Mott-Schottky plots analyzed at 500 and 1000 Hz are displayed in panels (b) and (c) of Figure 7, respectively. The flat band potentials ( $V_{fb}$ ) of MIL-101(Cr) and SnO<sub>2</sub> were  $-0.95$  and  $-0.25$  eV vs. the Ag/AgCl electrode, respectively. Transforming the difference between the Ag/AgCl electrode and the standard hydrogen electrode, the CB positions of the samples were finally calculated as  $-0.75$  and  $-0.05$  eV, respectively (vs. NHE, pH = 7).

The VBs of the samples were measured from the VB-XPS plots. Panels (d) and (e) of Figure 7 display the VB-XPS spectra of MIL-101(Cr) and SnO<sub>2</sub>, respectively, from which the VBs were determined as 1.77 and 4.05 eV, respectively. The VB potential of the normal hydrogen electrode ( $E_{VB-NHE}$ , vs. NHE, pH = 7) was calculated as the contact potential difference between the sample and the XPS analyzer, namely, as  $E_{VB-NHE} = \phi + E_{VB-XPS} - 4.44$  [23]. Here,  $\phi$  is the electron work function (4.55 eV) of the XPS analyzer, and  $E_{VB-XPS}$  is the VB measured from the VB-XPS plots. By this equation, the  $E_{VB-NHE}$  values of MIL-101(Cr) and SnO<sub>2</sub> were calculated as 1.88 and 4.16 eV, respectively. From the Mott-Schottky and XPS spectral analyses, the calculated bandgaps of MIL-101(Cr) and SnO<sub>2</sub> were 2.63 and 4.21 eV, respectively.

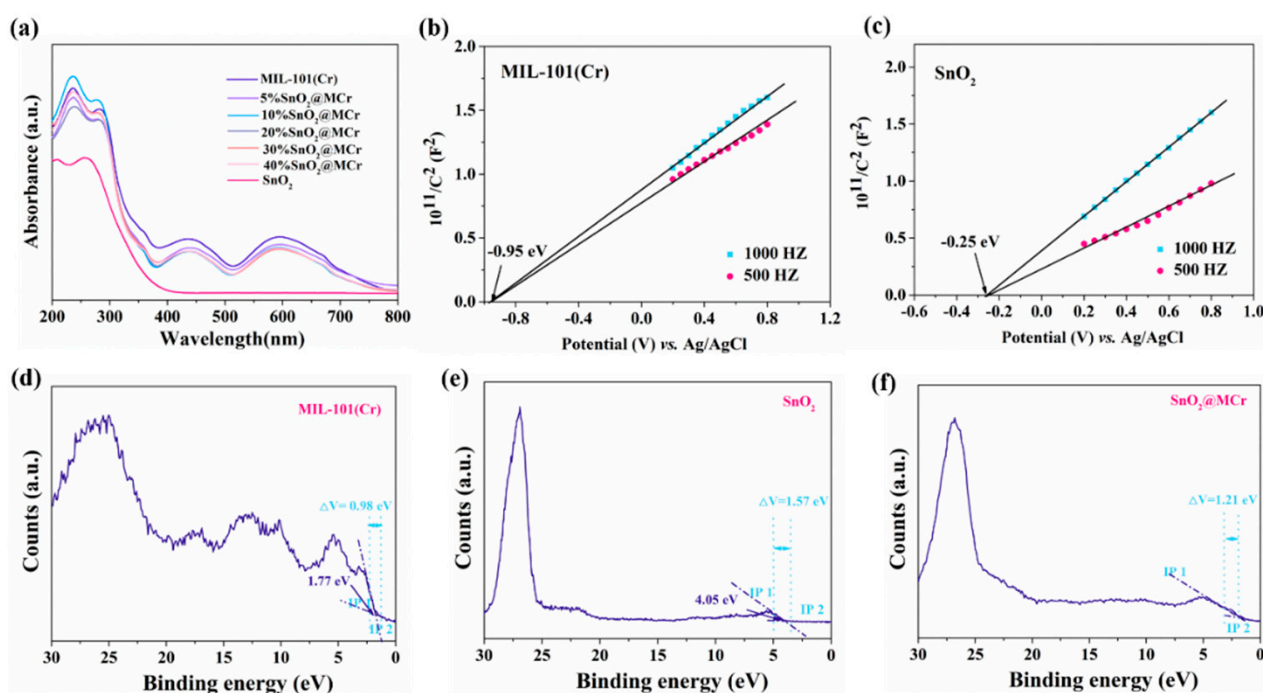


**Figure 7.** (a) UV–Vis diffuse reflection spectra of the as-prepared samples. (b) Mott–Schottky plots of (MIL-101(Cr) and (c) SnO<sub>2</sub>. Valence band (VB)–XPS curves of (d) MIL-101(Cr), (e) SnO<sub>2</sub>, and (f) 20%SnO<sub>2</sub>@MCR.

To further explore the interfacial charge transfer between MIL-101(Cr) and SnO<sub>2</sub>, the work functions of MIL-101(Cr), SnO<sub>2</sub>, and SnO<sub>2</sub>@MCR were measured and calculated from the VB–XPS plots. When the solid sample made good electrical contact with the metal sample holder of the XPS analyzer and the electron transfer was balanced, the Fermi levels of the solid sample and metal holder reached the same level. However, as the work functions differed between the two materials, the kinetic energy of the free electrons was changed by the contact potential difference  $\Delta V = \Phi - \varphi$  (where  $\varphi = 4.55$  eV is the work function of the XPS analyzer, and  $\Phi$  is the work function of the sample), thereby changing the binding energy of the electrons [39]. After measuring the binding energy changes over a small range by XPS,  $\Delta V$  was obtained from the spacing between the two inflection points of the curves (Figure 7d–f). The  $\Phi$ s of MIL-101(Cr), SnO<sub>2</sub>, and SnO<sub>2</sub>@MCR were thus calculated as 5.53, 6.02, and 5.76 eV, respectively. Figure 8 displays the band structures and work functions of MIL-101(Cr) and SnO<sub>2</sub> before and after contact, derived from the above-obtained Mott–Schottky and VB XPS values. MIL-101(Cr) was identified as a reduction-type photocatalyst with a lower work function (5.53 eV) and a higher Fermi level ( $E_f$ ), whereas SnO<sub>2</sub> was an oxidation-type photocatalyst with a higher work function (6.02 eV) and lower  $E_f$ . When MIL-101(Cr) and SnO<sub>2</sub> were in contact, electrons were transferred from MIL-101(Cr) to SnO<sub>2</sub> until the  $E_f$  values were equalized. At this time, an internal electric field from MIL-101(Cr) to SnO<sub>2</sub> formed at the interface. Once irradiated with light, the electrons in the CB of SnO<sub>2</sub> recombined with the holes in the VB of MIL-101(Cr); meanwhile, the holes of SnO<sub>2</sub> with a strong oxidation capacity and the photogenerated electrons of MIL-101(Cr) with a strong reduction capacity remained in their energy bands, greatly promoting the redox ability of the S-scheme SnO<sub>2</sub>@MCR photocatalyst.

## 2.2. Adsorption Performance

Substrate adsorption and mass transmission are essential in the photocatalytic process. Therefore, pyridine adsorption experiments were carried out using MIL-101(Cr), SnO<sub>2</sub>, and 20%SnO<sub>2</sub>@MCR as adsorbents. The SnO<sub>2</sub> nanoparticles were almost unable to adsorb pyridine, whereas the MIL-101(Cr) exhibited a 38.8% removal efficiency for pyridine (Figure S4). After being coated with SnO<sub>2</sub> QDs, the removal efficiency for pyridine decreased to 15.4%,



which can be ascribed to acid–base interactions (chemical adsorption) and pore-adsorption interactions (physical adsorption) between MIL-101(Cr) and the pyridine molecules.

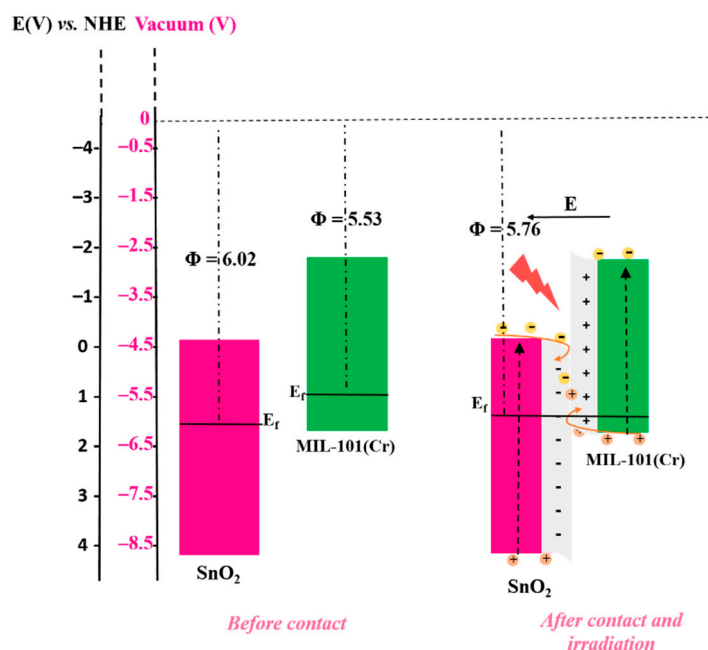


**Figure 8.** Energy diagrams of MIL-101(Cr) and SnO<sub>2</sub> before and after contact, and the formation of an internal electric field.

To further understand the interaction mechanisms between the representative organic molecules and the SnO<sub>2</sub>@MCr surface, high-resolution Cr and Sn spectra were obtained (presented in Figure 9). The Cr 2p bands of the bare SnO<sub>2</sub>@MCr surface at 577.75 and 587.26 eV were ascribed to Cr 2p<sub>3/2</sub> and Cr 2p<sub>1/2</sub>, respectively (Figure 9a). After treating the MIL-101(Cr) surface with pyridine, the Cr 2p<sub>3/2</sub> and Cr 2p<sub>1/2</sub> bands shifted to 577.23 and 586.95 eV, respectively. Meanwhile, pyridine adsorption did not significantly influence the Sn 3d<sub>5/2</sub> and Sn 3d<sub>3/2</sub> peaks in the spectrum of SnO<sub>2</sub>@MCr (Figure 9b). These results prove that pyridine strongly adsorbed on the SnO<sub>2</sub>@MCr surface and the main binding sites were derived from Cr<sup>3+</sup>.

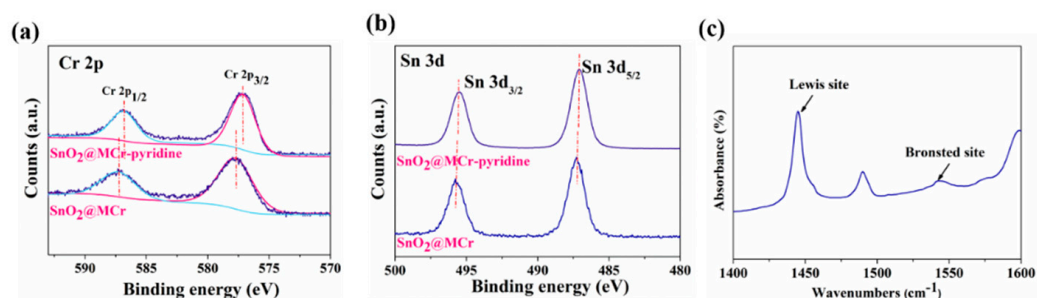


**Figure 9.** XPS survey spectra: (a) Cr 2p spectra and (b) Sn 3d spectra of 20%SnO<sub>2</sub>@MCr before and after adsorption of pyridine; (c) Fourier transform infrared spectrum of 20%SnO<sub>2</sub>@MCr during pyridine adsorption.

To determine the acidities of the samples, pyridine adsorption was monitored by FTIR (FTIR-pyridine). In the FTIR-pyridine spectrum of 20%SnO<sub>2</sub>@MCr, the sharp peaks at 1450 cm<sup>-1</sup> indicate the presence of Lewis-acidic uncoordinated octahedral Cr<sup>3+</sup> sites (Figure 9c). The peak at 1540 cm<sup>-1</sup> was ascribed to Brønsted acid sites contributed to by uncoordinated water molecules of MIL-101(Cr) (forming protonated pyridine, PyH<sup>+</sup>) [40]. The concentrations of the Lewis and Brønsted acid sites in 20%SnO<sub>2</sub>@MCr were 108.7 and

15.1  $\mu\text{mol/g}$ , respectively, suggesting a mixed acidity in 20%SnO<sub>2</sub>@MCr with dominant Lewis acidity. Moreover, the Cr<sup>3+</sup> central metal in SnO<sub>2</sub>@MCr was predicted as a Lewis acid, which can combine with pyridine (a Lewis base). Therefore, Cr and N might interact during the pyridine adsorption process over SnO<sub>2</sub>@MCr. The above analysis showed the strong pyridine binding affinity of MIL-101(Cr), while the synergistic effect of MIL-101(Cr) and SnO<sub>2</sub> ensured the high-efficiency denitrification of pyridine over the SnO<sub>2</sub>@MCr nanocomposite.

### 2.3. Photocatalytic Properties

The photocatalytic activity of SnO<sub>2</sub>@MCr was evaluated during photocatalytic denitrification of pyridine under simulated sunlight irradiation. First, the photocatalytic nature of the reaction was demonstrated in blank experiments (Figure 10a). The pyridine denitrogenation hardly occurred in the absence of light or photocatalyst. The denitrogenation abilities of pristine SnO<sub>2</sub> and MIL-101(Cr) were relatively weak, and the pyridine concentration changes were small. In contrast, the pyridine denitrogenation proceeded smoothly in the presence of SnO<sub>2</sub>@MCr. In the sample containing 20 wt.% SnO<sub>2</sub>, the photo-denitrification efficiency rapidly increased (to 90.1%) after four hours of simulated sunlight irradiation. To check the synergetic effect, the photocatalytic activity of SnO<sub>2</sub> + MIL-101(Cr) (prepared by simply mixing SnO<sub>2</sub> and MIL-101(Cr) in the proper proportions) was studied under the same condition. In this mixture, 65.0% of the pyridine was denitrogenated after four hours of sunlight irradiation, further confirming that the SnO<sub>2</sub>@MCr heterojunction supported carrier transfer between the interface of SnO<sub>2</sub> and MIL-101(Cr), thus improving the photocatalytic degradation efficiency. However, increasing the SnO<sub>2</sub> content beyond 20 wt.% reduced the photocatalytic performance. As evidenced in Figure 10b, the denitrification efficiency for pyridine decreased from 90.1% to 61.0%. This result is reasonable, because an excessively high SnO<sub>2</sub> content not only facilitates agglomeration of the SnO<sub>2</sub> particles, but also shields the active sites on MIL-101(Cr) [30]. To understand the reaction kinetics of the photocatalytic pyridine denitrification, the reaction rate constant  $k$  was calculated from the expression  $\ln(C_t/C_0) = -kt$ , which assumes a pseudo first-order reaction. Here,  $C_0$  and  $C_t$  denote the pyridine concentrations at times 0 and  $t$ , respectively. Under simulated sunlight irradiation, the 20%SnO<sub>2</sub>@MCr photocatalyst achieved a pyridine denitrification  $k$  of 0.5012 h<sup>-1</sup>, higher than those of MIL-101(Cr) (0.1888 h<sup>-1</sup>), SnO<sub>2</sub> (0.2275 h<sup>-1</sup>), and SnO<sub>2</sub>+MIL-101(Cr) (0.2229 h<sup>-1</sup>) (Figure 10c,d). A comparison between the photocatalytic activity of our 20%SnO<sub>2</sub>@MCr and that of other reported catalysts is listed in Table 3. It is worth noting that, compared with some of photocatalysts, the 20%SnO<sub>2</sub>@MCr exhibits better or comparable photocatalytic activity for the pyridine denitrogenation under visible light irradiation [2,4–7,41,42].

**Table 3.** Comparison between the photocatalytic activity of 20%SnO<sub>2</sub>@MCr and that of other reported catalysts for pyridine denitrogenation.

Photocatalysts	C <sub>pyridine</sub> ( $\mu\text{g/g}$ )	C <sub>cat</sub> (mg/mL)	Light Source	Denitrogenation Efficiency	Ref.
20%SnO <sub>2</sub> @MCr	100	0.5	300 W (280 nm < $\lambda$ < 980 nm)	4.0 h, 95%	This work
0.25%SDS/Fe <sub>2</sub> O <sub>3</sub> -450	100	1.0	300 W ( $\lambda$ > 420 nm)	4.0 h, 99%	[2]
Bi <sub>20</sub> TiO <sub>32</sub>	100	1.0	400 W ( $\lambda$ > 400 nm)	2.5 h, 81%	[4]
TiO <sub>2</sub> /Fe <sub>2</sub> O <sub>3</sub>	100	1.0	400 W ( $\lambda$ > 420 nm)	4.0 h, 92%	[5]
Bi <sub>2</sub> MoO <sub>6</sub> /CdS	100	1.0	300 W ( $\lambda$ > 420 nm)	4.0 h, 81%	[6]
CdS/Pt/Bi <sub>2</sub> MoO <sub>6</sub>	150	1.0	300 W ( $\lambda$ > 420 nm)	4.0 h, 94%	[7]
CeO <sub>2</sub> /TiO <sub>2</sub>	100	1.0	400 W ( $\lambda$ > 400 nm)	2.5 h, 76%	[41]
g-C <sub>3</sub> N <sub>4</sub>	130	5.0	500 W ( $\lambda$ > 400 nm)	6.0 h, 91%	[42]

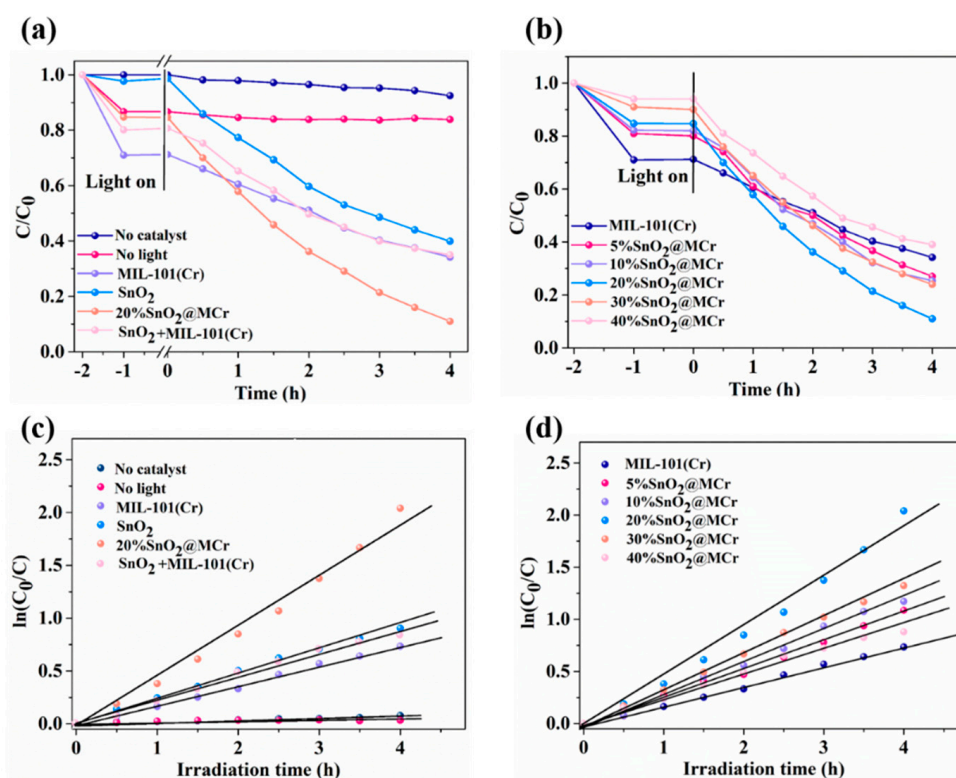


**Figure 10.** (a,b) Photocatalytic denitrification curves of pyridine over MIL-101(Cr), SnO<sub>2</sub>, and SnO<sub>2</sub>@MCr under simulated sunlight irradiation; (c,d) pseudo-first-order reaction kinetics of the samples in the photocatalytic denitrification of pyridine. Reaction conditions: 25 mg photocatalyst in 50 mL of 100  $\mu\text{g/g}$  pyridine/octane solution.

Reusability is another important property of a practical photocatalyst. The 20%SnO<sub>2</sub>@MCr photocatalyst delivered a stable performance with no noticeable deactivation over five cycles of photocatalytic experiments (Figure 11a). Powder XRD patterns and TEM images confirmed that the composition and morphology of 20%SnO<sub>2</sub>@MCr were well preserved after the photocatalysis (Figure 11b–e), affirming the excellent long-term durability of the photocatalyst under simulated sunlight irradiation. The intermediate products of pyridine denitrification were then determined by high-performance liquid chromatography (HPLC)–MS analysis (see Figure S5). Under irradiation for four hours, the peak intensity of pyridine ( $m/z \sim 80$ ) was greatly decreased, implying the successful denitrogenation of pyridine. Meanwhile, two new peaks gradually appeared at  $m/z = 64$  and  $m/z = 58$ , suggesting that pyridine was transformed into protonated intermediate products and was ultimately mineralized into inorganic products such as CO<sub>2</sub> and NO<sub>3</sub><sup>−</sup>, again consistent with our previous results [2,7].

#### 2.4. Possible Photocatalytic Mechanism

The generation of various oxidative species over the 20%SnO<sub>2</sub>@MCr photocatalyst was probed by the electron spin resonance (ESR) technique [43,44]. The characteristic peaks of DMPO- $\bullet\text{O}_2^-$  and DMPO- $\bullet\text{OH}$  were not observed under dark conditions but appeared under light irradiation (Figure 12a,b). Judging from this result,  $\bullet\text{O}_2^-$  and  $\bullet\text{OH}$  were the main active species. The generated  $\text{h}^+$  were investigated using 2,2,6,6-tetramethylpiperidinyl-1-oxyl (TEMPO) as the hole probe because its radical can be oxidized by  $\text{h}^+$ . As shown in Figure 12c, the characteristic TEMPO peak was strong under dark conditions and significantly decreased with increasing irradiation time, confirming that holes were photogenerated during pyridine denitrification. The above experiments prove that the main active species in the 20%SnO<sub>2</sub>@MCr S-scheme heterostructure are  $\bullet\text{O}_2^-$ ,  $\bullet\text{OH}$ , and  $\text{h}^+$ , further affirming the forming of the S-scheme heterojunction in this SnO<sub>2</sub>@MCr system.

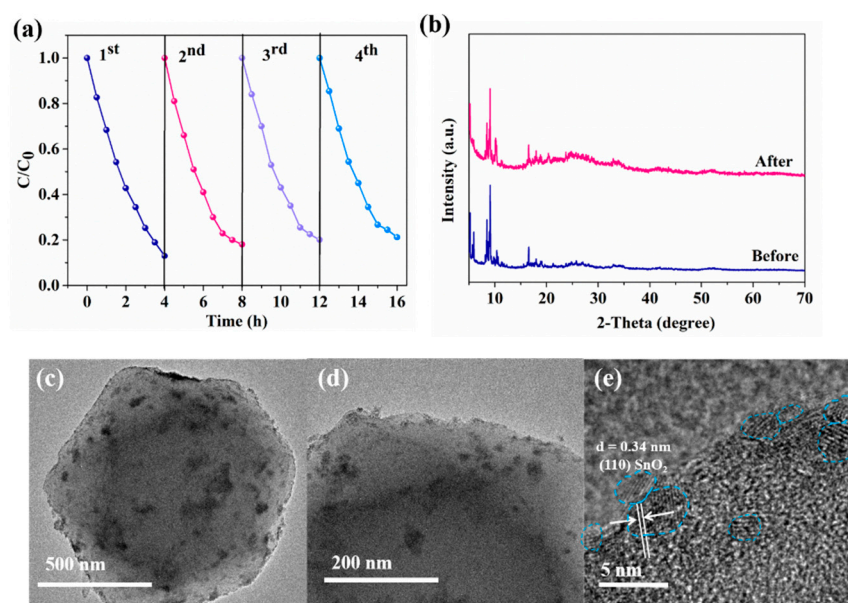


**Figure 11.** (a) Cycled experimental results of 20% $\text{SnO}_2$ @MCr, (b) XRD patterns, and (c–e) TEM analyses of 20% $\text{SnO}_2$ @MCr before and after the reaction.

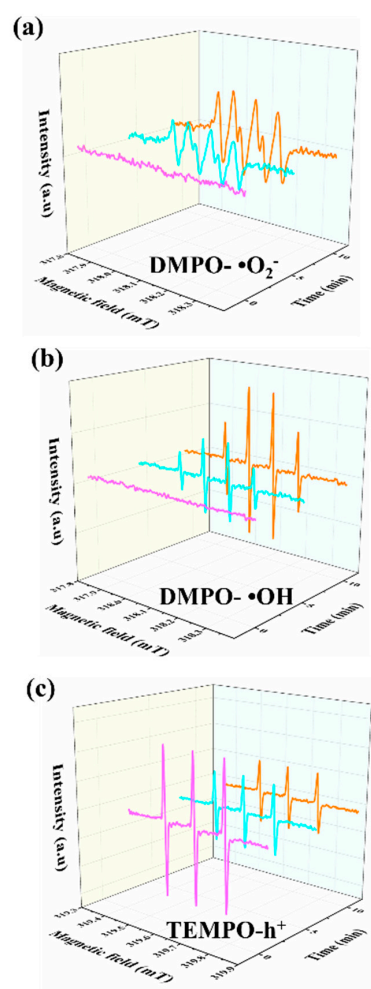


**Figure 12.** ESR spectra of various radical adducts (a)  $\text{DMPO}\cdot\text{O}_2^-$ , (b)  $\text{DMPO}\cdot\text{OH}$ , (c)  $\text{TEMPO}\cdot\text{h}^+$ .



The photogenerated carrier separation ability in 20%SnO<sub>2</sub>@MCr was evaluated in a photocurrent response and electrochemical impedance spectroscopy analysis. Figure 13a displays the transient photocurrent responses of MIL-101(Cr), SnO<sub>2</sub>, and 20%SnO<sub>2</sub>@MCr during several on–off cycles under simulated sunlight irradiation. The current generation implied that electron–hole pairs were separated under the simulated sunlight irradiation, whereas the current decay indicated recombination of the photogenerated carriers. The 20%SnO<sub>2</sub>@MCr sample achieved a clearly higher photocurrent intensity than pure MIL-101(Cr) and SnO<sub>2</sub>, implying that this composite optimally separated and transferred the carriers. Figure 13b shows typical Nyquist plots of the prepared samples obtained in the dark. The smaller radius of 20%SnO<sub>2</sub>@MCr than of the pure substances indicates a small charge-transfer impedance and a high charge separation in the composite. In summary, the 20%SnO<sub>2</sub>@MCr sample achieved the largest photocurrent and the smallest electrical impedance among the prepared samples, indicating that it optimized the photocatalytic performance, as shown in the previous photoactivity test results.

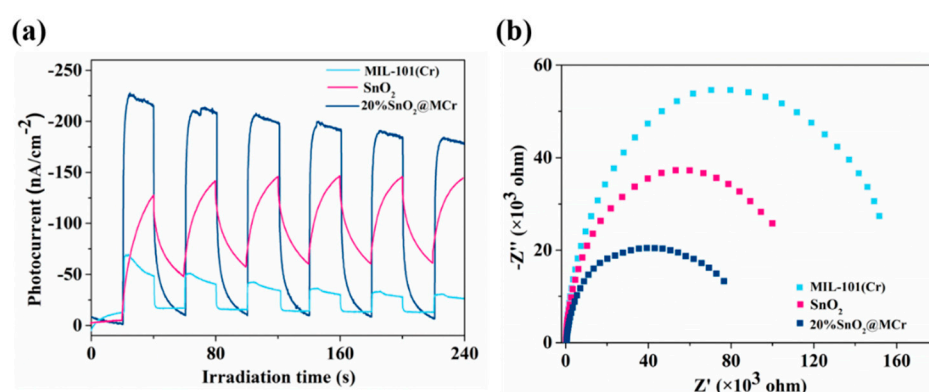
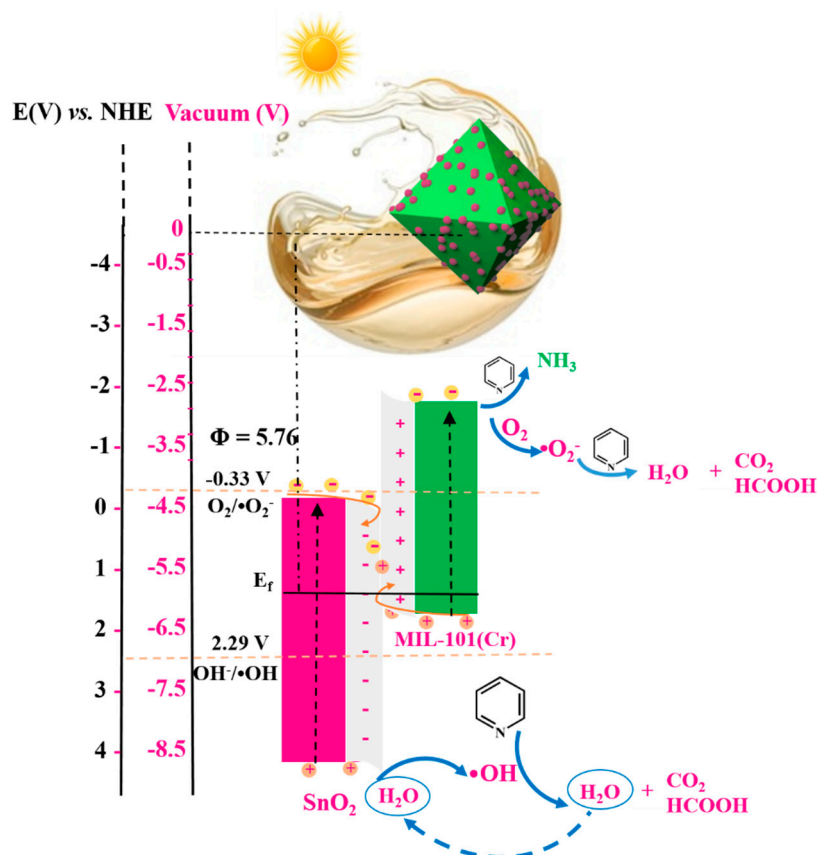


**Figure 13.** (a) Transient photocurrent responses of MIL-101(Cr), SnO<sub>2</sub>, and 20%SnO<sub>2</sub>@MCr in 0.5 M Na<sub>2</sub>SO<sub>4</sub> aqueous solution under simulated sunlight irradiation; (b) Nyquist plots of the samples.

Based on the above results, the possible scheme of pyridine denitrogenation by SnO<sub>2</sub>@MCr was proposed as Scheme 2. The band structure suggested that the SnO<sub>2</sub>@MCr heterojunction was a typical II-type heterojunction. However, if SnO<sub>2</sub>@MCr obeyed the II-type mechanism, the electrons of MIL-101(Cr) could be injected into the CB of SnO<sub>2</sub> (with an energy of  $-0.03$  eV), and the holes of SnO<sub>2</sub> could migrate to MIL-101(Cr) (with a VB energy of only  $1.88$  eV). These photogenerated electrons and holes would have lower reducing and oxidizing abilities to generate  $\bullet\text{O}_2^-$  ( $\text{O}_2/\bullet\text{O}_2^-$ ,  $-0.33$  eV) and  $\bullet\text{OH}$  ( $\text{OH}^-/\bullet\text{OH}$ ,  $2.29$  eV), which clearly contradicts the above experimental results. Combining the above-discussed energy band structures, internal electric fields, and free radical testing results, the most reasonable photocatalytic charge-transfer mechanism of this experimental system was the S-scheme photocatalytic mechanism. In particular, the formation of a novel S-scheme SnO<sub>2</sub>@MCr heterojunction was facilitated by the large contact area and the Fermi-level difference between SnO<sub>2</sub> and MIL-101(Cr). The relatively useless electrons (from the CB of SnO<sub>2</sub>) and holes (from the VB of MIL-101(Cr)) recombined, while the useful holes and electrons were retained. The enhanced redox potential at the VB of SnO<sub>2</sub> and the CB of MIL-101(Cr) enabled the oxidation of H<sub>2</sub>O to  $\bullet\text{OH}$  and the reduction of O<sub>2</sub> to  $\bullet\text{O}_2^-$ , respectively. The generated holes,  $\bullet\text{OH}$ , and  $\bullet\text{O}_2^-$ , were the main active species that reacted with the pyridine molecules adsorbed on the SnO<sub>2</sub>@MCr surface.



**Scheme 2.** Schematic of photocatalytic pyridine denitrification over the  $\text{SnO}_2\text{@MIL-101(Cr)}$  composite.

### 3. Materials and Methods

#### 3.1. Materials

All reagents were analytical grade and used without further purification. Chromium nitrate ( $\text{Cr}(\text{NO}_3)_3 \cdot 9\text{H}_2\text{O}$ , 99 wt%), stannic chloride ( $\text{SnCl}_4 \cdot 5\text{H}_2\text{O}$ , 99 wt%), hydrofluoric acid (HF, 49%), anhydrous ethanol (99.5 wt%), pyridine (99.5 wt%), and octane (99.5 wt%) were purchased from Sinopharm Chemical Reagent Co. Ltd., China. Terephthalic acid ( $\text{H}_2\text{BDC}$ , 99 wt%) was supplied by Alfa Aesar China Co., Ltd. (Tianjin, China).

#### 3.2. Synthesis of MIL-101(Cr)

MIL-101(Cr) was synthesized via a modified hydrothermal method reported by G. Férey [28]. Briefly,  $\text{Cr}(\text{NO}_3)_3 \cdot 9\text{H}_2\text{O}$  (4.00 g),  $\text{H}_2\text{BDC}$  (1.64 g), HF (0.1 mL), and deionized water (48 mL) were added to a 100 mL Teflon-lined autoclave, and the mixture was heated at  $220^\circ\text{C}$  for 8 h. After cooling down to room temperature, the product was collected by centrifugation and then further washed with hot ethanol and deionized water to remove the unreacted  $\text{H}_2\text{BDC}$ . Finally, the obtained pale green powder was dried overnight at  $80^\circ\text{C}$ .

#### 3.3. Synthesis of $\text{SnO}_2\text{@MIL-101(Cr)}$ ( $\text{SnO}_2\text{@MIL-101(Cr)}$ )

As shown in Scheme 1, the  $\text{SnO}_2\text{@MIL-101(Cr)}$  hybrids were synthesized by a simple hydrothermal method. Typically, a certain amount of  $\text{SnCl}_4 \cdot 5\text{H}_2\text{O}$  (0.0582, 0.1164, 0.2327, 0.3492, 0.4656 g), 500 mg of MIL-101(Cr) powder, and 50 mL of deionized water were added to a 100 mL Teflon-lined autoclave and the mixture was heated at  $160^\circ\text{C}$  for 10 h. After being cooled to room temperature, the crude product was obtained by centrifugation and then further washed with deionized water and ethanol several times. The obtained pale green powder was dried overnight at  $60^\circ\text{C}$ . The loading of  $\text{SnO}_2$  in the composites was about 5, 10, 20, 30, and 40 wt.% for 0.0582, 0.1164, 0.2327, 0.3492, and 0.4656 g of  $\text{SnCl}_4 \cdot 5\text{H}_2\text{O}$ , designated as sample 5% $\text{SnO}_2\text{@MIL-101(Cr)}$ , 10% $\text{SnO}_2\text{@MIL-101(Cr)}$ , 20% $\text{SnO}_2\text{@MIL-101(Cr)}$ , 30% $\text{SnO}_2\text{@MIL-101(Cr)}$ , and

40%SnO<sub>2</sub>@MCr, respectively. The bare SnO<sub>2</sub> without adding MIL-101(Cr) was prepared through the same procedure.

### 3.4. Characterizations

XRD patterns were carried on a Bruker D8 Advance X-ray diffractometer operated at 40 kV and 40 mA with Ni-filtered Cu Ka irradiation ( $\lambda = 0.15406$  nm). The size and the morphology of the samples were determined by scanning electron microscopy (SEM) using a Hitachi SU8000 scanning microscope. Transmission electron microscopy (TEM) and high-resolution transmission electron microscopy (HRTEM) images were obtained using a JEOL model JEM 2010 EX instrument at an accelerating voltage of 200 kV. UV-vis diffuse reflectance spectra (UV-vis DRS) were obtained using a UV-vis spectrophotometer (Varian Cary 500). The Brunauer–Emmett–Teller (BET) surface area was measured with an ASAP2020M apparatus (Micromeritics Instrument Corp., USA). X-ray photo electron spectroscopy (XPS) measurement was performed with a Thermo Scientific ESCA Lab 250 spectrometer. The electron spin response (ESR) experiment was carried out with a Bruker 300 spectrometer. The photoluminescence spectra (PL) of all samples were tested using a fluorescence spectrometer (FLS 980). The photocurrent measurements were conducted with a BAS Epsilon workstation. The Mott–Schottky experiments were conducted on a Precision PARC workstation using electro chemical impedance spectroscopy (EIS). Fourier transform infrared spectroscopy (FTIR) with pyridine as the probe molecule was performed using a Nicolet 6700 to identify the Brønsted and Lewis acid sites. The samples were first degassed at 180 °C for 2 h, followed by pyridine adsorption at 25 °C for 1 h. Removal of physisorbed pyridine was performed at 150 °C for 30 min, and the spectra was collected after conducting desorption at 150 °C for 1 h. The liquid chromatograph-mass spectrometer (HPLC-MS) method for analyzing pyridine was performed using an Agilent 1200 series (Palo Alto, CA, USA) equipped with an Agilent Zorbax Eclipse XDB-C18 column (2.1 mm  $\times$  100 mm, 3.5  $\mu$ m). The column was maintained at 30 °C during the sample analysis. The measurement for pyridine was performed in an isocratic elution program with methanol/acetone = 70:30 (*v/v*) as the mobile phase. Flow rate was kept at 0.2 mL/min, and the injection volume was 10  $\mu$ L.

### 3.5. Evaluation of Photocatalytic Activity

The photocatalytic activity of SnO<sub>2</sub>@MCr composites was studied through the photocatalytic denitrification of pyridine under simulated sunlight irradiation. In detail, the photocatalytic denitrification of pyridine was carried out at 30 °C in a 100 mL quartz reactor containing 25 mg of SnO<sub>2</sub>@MCr and 50 mL of pyridine/octane solution (100  $\mu$ g/g). The simulated NCCs-containing gasoline fuel (100  $\mu$ g/g) was prepared by dissolving 70 mg of pyridine in 1.0 L of octane. The suspension was stirred in the dark for 2 h to ensure the establishment of adsorption–desorption equilibrium. The suspensions were irradiated by a 300 W Xe lamp (PLS-SXE 300, Beijing Perfectlight Co. Ltd., 280 nm  $< \lambda <$  980 nm), and the distance between them was 10 cm. During illumination, 2 mL of suspension was taken from the reactor at scheduled intervals and centrifuged to separate the photocatalyst. The pyridine content in the supernatant solution was determined colorimetrically at 251 nm using a Cary 50 UV-vis spectrophotometer (Varian Co.).

## 4. Conclusions

In summary, a novel SnO<sub>2</sub>@MCr photocatalyst was synthesized via a simple hydrothermal strategy. In this architecture, the highly dispersed SnO<sub>2</sub> QDs with the size of  $\sim$ 3 nm were evenly distributed on the MIL-101(Cr). Moreover, because of the differences of Fermi level and band structure of the SnO<sub>2</sub> and MIL-101(Cr), an S-scheme heterojunction could be established. The obtained SnO<sub>2</sub>@MCr hybrid exhibited high photocatalytic performances for pyridine denitrification. In particular, after sunlight irradiation for 4 h, 20%SnO<sub>2</sub>@MCr could result in 95% pyridine denitrification, with a corresponding *k* value of 0.5012 h<sup>−1</sup>. After four cycles of pyridine denitrification, the photocatalytic properties, crystal structure,

and microstructure of the composite were maintained, indicating the excellent stability and reusability of SnO<sub>2</sub>@MCR composites. In addition, the possible photocatalytic mechanism of pyridine was elucidated through the systematic characterization results. In addition, it was pointed out that the oxidative radicals, such as holes, •OH and •O<sub>2</sub><sup>−</sup> were the main reaction species for pyridine denitrification. In addition, the TiO<sub>2</sub> amount, initial pH value, catalyst dosage, and initial BPA concentration influenced the degradation of BPA. The improvement in photocatalytic activity is attributed to (i) the high dispersion of SnO<sub>2</sub> QDs, (ii) the binding of the rich adsorption sites with pyridine molecules. and (iii) the formation of the S-scheme heterojunction between SnO<sub>2</sub> and MIL-101(Cr). Finally, the synergistic effect of coordination adsorption-photocatalysis, the possible degradation pathways, and the degradation mechanism were proposed. This work not only demonstrates the immense potential of MOFs in photocatalysis but also provides a specimen for further fabrication and design of MOFs-based S-scheme heterojunctions that could be used for effectively removing NCCs in crude gasoline fuel.

**Supplementary Materials:** The following are available online: Figure S1: FTIR patterns of MIL-101(Cr), SnO<sub>2</sub>, and 20%SnO<sub>2</sub>@MCR; Figure S2: (a) EDS spectrum, (b–g) EDS elemental mappings for the sample of 20%SnO<sub>2</sub>@MCR; Figure S3: (a) Nitrogen sorption isotherms, (b) pore size distribution of SnO<sub>2</sub>; Figure S4: Adsorption capacity of SnO<sub>2</sub>@MCR towards pyridine, reaction conditions: 25 mg of photocatalyst and 50 mL of 100 µg/g pyridine/octane solution; Figure S5: HPLC-MS spectrogram of RhB degradation over 30%AgBr-1.5%Ag@MFe composites at different reaction times: (a) 0 h, (b) 2.0 h, and (c) 4.0 h.

**Author Contributions:** Conceptualization: Y.X., Z.L. and L.W.; investigation: R.L., Y.L., S.W., Z.H. and G.Y.; writing—review and editing: R.L. All authors have read and agreed to the published version of the manuscript.

**Funding:** This work was supported by the National Natural Science Foundation of China (21806085, 22108129), the Natural Science Foundation of Fujian Province (2019J01837), and the Natural Science Foundation of Ningde Normal University (2020T01, 2019ZX410). Moreover, we are also grateful to the Program of IRTSTFJ for their financial support.

**Institutional Review Board Statement:** Not applicable.

**Informed Consent Statement:** Not applicable.

**Data Availability Statement:** The data presented in the study are available from the corresponding author.

**Conflicts of Interest:** The authors declare no conflict of interest.

**Sample Availability:** Not applicable.

## References

1. Mondol, M.M.H.; Bhadra, B.N.; Jhung, S.H. Removal of nitrogen-containing compounds from microalgae derived biofuel by adsorption over functionalized metal organic frameworks. *Fuel* **2020**, *280*, 118622. [[CrossRef](#)]
2. Liang, R.; Liang, Z.; Chen, F.; Xie, D.; Wu, Y.; Wang, X.; Yan, G.; Wu, L. Sodium dodecyl sulfate-decorated MOF-derived porous Fe<sub>2</sub>O<sub>3</sub> nanoparticles: High performance, recyclable photocatalysts for fuel denitrification. *Chin. J. Catal.* **2020**, *41*, 188–199. [[CrossRef](#)]
3. Yao, H.; Wang, G.; Zuo, C.; Li, C.; Wang, E.; Zhang, S. Deep hydrodenitrification of pyridine by solid catalyst coupling with ionic liquids under mild conditions. *Green Chem.* **2017**, *19*, 1692–1700. [[CrossRef](#)]
4. Zheng, L.; Yan, G.; Huang, Y.; Wang, X.; Long, J.; Li, L.; Xu, T. Visible-light photocatalytic denitrogenation of nitrogen-containing compound in petroleum by metastable Bi<sub>20</sub>TiO<sub>32</sub>. *Int. J. Hydrog. Energy.* **2014**, *39*, 13401–13407. [[CrossRef](#)]
5. Huang, R.; Liang, R.; Fan, H.; Ying, S.; Wu, L.; Wang, X.; Yan, G. Enhanced photocatalytic fuel denitrification over TiO<sub>2</sub>/α-Fe<sub>2</sub>O<sub>3</sub> nanocomposites under visible light irradiation. *Sci. Rep.* **2017**, *7*, 7858. [[CrossRef](#)] [[PubMed](#)]
6. Hu, W.; Jiang, M.; Liang, R.; Huang, R.; Xia, Y.; Liang, Z.; Yan, G. Construction of Bi<sub>2</sub>MoO<sub>6</sub>/CdS heterostructures with enhanced visible light photocatalytic activity for fuel denitrification. *Dalton Trans.* **2021**, *50*, 2596–2605. [[CrossRef](#)] [[PubMed](#)]
7. Hu, W.; Yan, G.; Liang, R.; Jiang, M.; Huang, R.; Xia, Y.; Chen, L.; Lu, Y. Construction of a novel step-scheme CdS/Pt/Bi<sub>2</sub>MoO<sub>6</sub> photocatalyst for efficient photocatalytic fuel denitrification. *RSC Adv.* **2021**, *11*, 23288–23300. [[CrossRef](#)]
8. Stock, N.; Biswas, S. Synthesis of metal-organic frameworks (MOFs): Routes to various MOF topologies, morphologies, and composites. *Chem. Rev.* **2012**, *112*, 933–969. [[CrossRef](#)]



9. Wibowo, A.; Marsudi, M.A.; Pramono, E.; Belva, J.; Parmita, A.W.Y.P.; Patah, A.; Eddy, D.R.; Aimon, A.H.; Ramelan, A. Recent improvement strategies on metal-organic frameworks as adsorbent, catalyst, and membrane for wastewater treatment. *Molecules* **2021**, *26*, 5261. [[CrossRef](#)]
10. Chacón, P.; Hernández-Lima, J.G.; Bazán-Jiménez, A.; García-Revilla, M.A. Modeling adsorption and optical properties for the design of CO<sub>2</sub> photocatalytic metal-organic frameworks. *Molecules* **2021**, *26*, 3060. [[CrossRef](#)] [[PubMed](#)]
11. Liang, R.; He, Z.; Lu, Y.; Yan, G.; Wu, L. High-efficiency sandwich-like hierarchical AgBr-Ag@MIL-68(Fe) photocatalysts: Step-scheme photocatalytic mechanism for enhanced photoactivity. *Sep. Purif. Technol.* **2021**, *277*, 119442. [[CrossRef](#)]
12. Liang, R.; Huang, R.; Ying, S.; Wang, X.; Yan, G.; Wu, L. Facile in situ growth of highly dispersed palladium on phosphotungstic-acid-encapsulated MIL-100(Fe) for the degradation of pharmaceuticals and personal care products under visible light. *Nano Res.* **2018**, 1109–1123. [[CrossRef](#)]
13. Bordiga, S.; Lamberti, C.; Ricchiardi, G.; Regli, L.; Bonino, F.; Damin, A.; Lillerud, K.P.; Bjorgen, M.; Zecchina, A. Electronic and vibrational properties of a MOF-5 metal-organic framework: ZnO quantum dot behaviour. *Chem. Commun.* **2004**, 2300–2301. [[CrossRef](#)] [[PubMed](#)]
14. Cheng, X.-M.; Dao, X.-Y.; Wang, S.-Q.; Zhao, J.; Sun, W.-Y. Enhanced photocatalytic CO<sub>2</sub> reduction activity over NH<sub>2</sub>-MIL-125(Ti) by facet regulation. *ACS Catal.* **2021**, *11*, 650–658. [[CrossRef](#)]
15. Mu, F.; Dai, B.; Zhao, W.; Zhou, S.; Huang, H.; Yang, G.; Xia, D.; Kong, Y.; Leung, D.Y.C. Construction of a novel Ag/Ag<sub>3</sub>PO<sub>4</sub>/MIL-68(In)-NH<sub>2</sub> plasmonic heterojunction photocatalyst for high-efficiency photocatalysis. *J. Mater. Sci. Technol.* **2022**, *101*, 37–48. [[CrossRef](#)]
16. Zhang, Y.; Zhou, J.; Chen, J.; Feng, X.; Cai, W. Rapid degradation of tetracycline hydrochloride by heterogeneous photocatalysis coupling persulfate oxidation with MIL-53(Fe) under visible light irradiation. *J. Hazard. Mater.* **2020**, *392*, 122315. [[CrossRef](#)] [[PubMed](#)]
17. Chen, J.; Zhang, X.; Shi, X.; Bi, F.; Yang, Y.; Wang, Y. Synergistic effects of octahedral TiO<sub>2</sub>-MIL-101(Cr) with two heterojunctions for enhancing visible-light photocatalytic degradation of liquid tetracycline and gaseous toluene. *J. Colloid Interface Sci.* **2020**, *579*, 37–49. [[CrossRef](#)] [[PubMed](#)]
18. Zhao, S.-N.; Wang, G.; Poelman, D.; Van Der Voort, P. Metal organic frameworks based materials for heterogeneous photocatalysis. *Molecules* **2018**, *23*, 2947. [[CrossRef](#)]
19. Cortés-Villena, A.; Galian, R.E. Present and perspectives of photoactive porous composites based on semiconductor nanocrystals and metal-organic frameworks. *Molecules* **2021**, *26*, 5620. [[CrossRef](#)]
20. Xu, Q.; Zhang, L.; Cheng, B.; Fan, J.; Yu, J. S-Scheme heterojunction photocatalyst. *Chem* **2020**, *6*, 1543–1559. [[CrossRef](#)]
21. Ren, Y.; Li, Y.; Wu, X.; Wang, J.; Zhang, G. S-scheme Sb<sub>2</sub>WO<sub>6</sub>/g-C<sub>3</sub>N<sub>4</sub> photocatalysts with enhanced visible-light-induced photocatalytic NO oxidation performance. *Chin. J. Catal.* **2021**, *42*, 69–77. [[CrossRef](#)]
22. Wang, Y.; Wang, K.; Wang, J.; Wu, X.; Zhang, G. Sb<sub>2</sub>WO<sub>6</sub>/BiOBr 2D nanocomposite S-scheme photocatalyst for NO removal. *J. Mater. Sci. Technol.* **2020**, *56*, 236–243. [[CrossRef](#)]
23. Li, X.; Kang, B.; Dong, F.; Zhang, Z.; Luo, X.; Han, L.; Huang, J.; Feng, Z.; Chen, Z.; Xu, J.; et al. Enhanced photocatalytic degradation and H<sub>2</sub>/H<sub>2</sub>O<sub>2</sub> production performance of S-pCN/WO<sub>2.72</sub> S-scheme heterojunction with appropriate surface oxygen vacancies. *Nano Energy* **2021**, *81*, 105671. [[CrossRef](#)]
24. Puga, F.; Navío, J.A.; Hidalgo, M.C. Enhanced UV and visible light photocatalytic properties of synthesized AgBr/SnO<sub>2</sub> composites. *Sep. Purif. Technol.* **2021**, *257*, 117948. [[CrossRef](#)]
25. Sayadi, M.H.; Sobhani, S.; Shekari, H. Photocatalytic degradation of azithromycin using GO@Fe<sub>3</sub>O<sub>4</sub>/ZnO/SnO<sub>2</sub> nanocomposites. *J. Clean. Prod.* **2019**, *232*, 127–136. [[CrossRef](#)]
26. Gao, C.; Jiang, Z.; Wang, P.; Jensen, L.R.; Zhang, Y.; Yue, Y. Optimized assembling of MOF/SnO<sub>2</sub>/Graphene leads to superior anode for lithium ion batteries. *Nano Energy* **2020**, *74*, 104868. [[CrossRef](#)]
27. Mohanta, D.; Mahanta, A.; Mishra, S.R.; Jasimuddin, S.; Ahmaruzzaman, M. Novel SnO<sub>2</sub>@ZIF-8/gC<sub>3</sub>N<sub>4</sub> nano hybrids for excellent electrochemical performance towards sensing of p-nitrophenol. *Environ. Res.* **2021**, *197*, 111077. [[CrossRef](#)]
28. Férey, G.; Mellot-Draznieks, C.; Serre, C.; Millange, F.; Dutour, J.; Surblé, S.; Margiolaki, I. A Chromium Terephthalate-Based Solid with Unusually Large Pore Volumes and Surface Area. *Science* **2005**, *309*, 2040–2042. [[CrossRef](#)]
29. Du, P.D.; Thanh, H.T.M.; To, T.C.; Thang, H.S.; Tinh, M.X.; Tuyen, T.N.; Hoa, T.T.; Khieu, D.Q. Metal-organic framework MIL-101: Synthesis and photocatalytic degradation of remazol black B dye. *J. Nanomater.* **2019**, *2019*, 6061275. [[CrossRef](#)]
30. Gao, S.; Feng, T.; Feng, C.; Shang, N.; Wang, C. Novel visible-light-responsive Ag/AgCl@MIL-101 hybrid materials with synergistic photocatalytic activity. *J. Colloid. Interface Sci.* **2016**, *466*, 284–290. [[CrossRef](#)] [[PubMed](#)]
31. Wang, R.; Wu, L.; Chica, B.; Gu, L.; Xu, G.; Yuan, Y. Ni(dmgH)<sub>2</sub> complex coupled with metal-organic frameworks MIL-101(Cr) for photocatalytic H<sub>2</sub> evolution under visible light irradiation. *J. Mater.* **2017**, *3*, 58–62.
32. Gao, Y.; Mirante, F.; de Castro, B.; Zhao, J.; Cunha-Silva, L.; Balula, S.S. An effective hybrid heterogeneous catalyst to desulfurize diesel: Peroxotungstate@metal-organic framework. *Molecules* **2020**, *25*, 5494. [[CrossRef](#)] [[PubMed](#)]
33. Aziz, M.; Abbas, S.S.; Baharom, W.R.W.; Mahmud, W.Z.W. Structure of SnO<sub>2</sub> nanoparticles by sol-gel method. *Mater. Lett.* **2012**, *74*, 62–64. [[CrossRef](#)]
34. Tang, Y.; Yin, X.; Mu, M.; Jiang, Y.; Li, X.; Zhang, H.; Ouyang, T. Anatase TiO<sub>2</sub>@MIL-101(Cr) nanocomposite for photocatalytic degradation of bisphenol A. *Colloid Surf. A* **2020**, *596*, 124745. [[CrossRef](#)]

35. Ding, D.; Jiang, Z.; Jin, J.; Li, J.; Ji, D.; Zhang, Y.; Zan, L. Impregnation of semiconductor CdS NPs in MOFs cavities via double solvent method for effective photocatalytic CO<sub>2</sub> conversion. *J. Catal.* **2019**, *375*, 21–31. [[CrossRef](#)]
36. Xie, Q.; He, W.; Liu, S.; Li, C.; Zhang, J.; Wong, P.K. Bifunctional S-scheme g-C<sub>3</sub>N<sub>4</sub>/Bi/BiVO<sub>4</sub> hybrid photocatalysts toward artificial carbon cycling. *Chin. J. Catal.* **2020**, *41*, 140–153. [[CrossRef](#)]
37. Sheng, H.; Chen, D.; Li, N.; Xu, Q.; Li, H.; He, J.; Lu, J. Urchin-inspired TiO<sub>2</sub>@MIL-101 double-shell hollow particles: Adsorption and highly efficient photocatalytic degradation of hydrogen sulfide. *Chem. Mater.* **2017**, *29*, 5612–5616. [[CrossRef](#)]
38. Liang, R.; He, Z.; Zhou, C.; Yan, G.; Wu, L. MOF-derived porous Fe<sub>2</sub>O<sub>3</sub> nanoparticles coupled with CdS quantum dots for degradation of bisphenol A under visible light irradiation. *Nanomaterials* **2020**, *10*, 1701. [[CrossRef](#)] [[PubMed](#)]
39. Li, X.; Xiong, J.; Gao, X.; Ma, J.; Chen, Z.; Kang, B.; Liu, J.; Li, H.; Feng, Z.; Huang, J. Novel BP/BiOBr S-scheme nano-heterojunction for enhanced visible-light photocatalytic tetracycline removal and oxygen evolution activity. *J. Hazard. Mater.* **2020**, *387*, 121690. [[CrossRef](#)] [[PubMed](#)]
40. Chatterjee, A.; Hu, X.; Lam, F.L.-Y. Towards a recyclable MOF catalyst for efficient production of furfural. *Catal. Today* **2018**, *314*, 129–136. [[CrossRef](#)]
41. Chen, F.; Huang, Y.; Yan, G.; Fan, H.; Huang, R. Preparation and visible light denitrification performance of copper oxide/Zinc oxide/3A molecular sieve photocatalyst. *Chin. J. Appl. Chem.* **2015**, *32*, 1040–1047.
42. Zhang, X.; Song, H.; Sun, C.; Chen, C.; Han, F.; Li, X. Photocatalytic oxidative desulfurization and denitrogenation of fuels over sodium doped graphitic carbon nitride nanosheets under visible light irradiation. *Mater. Chem. Phys.* **2019**, *226*, 34–43. [[CrossRef](#)]
43. Kaushik, J.; Kumar, V.; Garg, A.K.; Dubey, P.; Tripathi, K.M.; Sonkar, S.K. Bio-mass derived functionalized graphene aerogel: A sustainable approach for the removal of multiple organic dyes and their mixtures. *New J. Chem.* **2021**, *45*, 9073–9083. [[CrossRef](#)]
44. Kaushik, J.; Himanshi; Kumar, V.; Tripathi, K.M.; Sonkar, S.K. Sunlight-promoted photodegradation of Congo red by cadmium-sulfide decorated graphene aerogel. *Chemosphere* **2022**, *287*, 132225. [[CrossRef](#)] [[PubMed](#)]